Proceedings of the ASME 2010 3rd Joint US-European Fluids Engineering Summer Meeting and 8th International Conference on Nanochannels, Microchannels, and Minichannels
FEDSM-ICNMM2010
August 1-5, 2010, Montreal, Canada

FEDSM-ICNMM2010-31298

FLOW INVESTIGATION IN A DISK MICROPUMP

André Lisibach
Department of Mechanical Engineering
Lucerne University of
Applied Sciences and Arts
Horw Switzerland
Email: lisibach@itp.phys.ethz.ch

Ernesto Casartelli
Department of Mechanical Engineering
Lucerne University
of Applied Sciences and Arts
Horw Switzerland
Email: ernesto.casartelli@hslu.ch

Noah Schmid
CSEM SA
Central Switzerland Center
Alpnach Switzerland
Email: Noa.SCHMID@csem.ch

ABSTRACT

The flow field in a disk micropump is investigated using CFD. The results are validated with experimental data, showing good agreement. Flow field details are presented for different pump parameters. In order to better understand the influence of the pump geometry and fluid properties on the pump performance, an analytical model for the pump head has been derived. Since the pumping mechanism is mainly due to viscous forces, a typical turbomachinery approach, which is based on the effect of centrifugal forces, is not appropriate. The proposed analytical model, which is general and can also be used for scale up purposes, shows that the non-dimensional results of CFD and measurements matches very well.

NOMENCLATURE

Q Massflow
η Dynamic viscosity
n Rotation speed
B Width of slit
ω Angular velocity
w Fluid velocity (absolute value)
ρ Fluid density
Re Reynold's number
r Radial coordinate
P Power
D, b Characteristic lengths (for dimensionless exposition)
F Force
M Torque
Y Specific Work
H_f Head
g Gravitational constant near earth surface
C_H, $C_{H,g}$ Dimensionless Head coefficient (g: including geometry)
C_Q, $C_{Q,g}$ Dimensionless massflow coefficient (g: including geometry)
R_1, R_2 Inner and outer Radius of the slit

Introduction

Micropumps are widely used for biomedical applications for a range of tasks (see for example [1], [2]). In this paper a disc micropump is analyzed. The disc pump is due to its linear and pulsation free behavior well suited for dosing applications. Diaphragm-, peristaltic-, gearwheel-pumps and even syringe pumps which are typically applied in dosing applications inherently always deal with a certain degree of a pulsating flow rate. In addition, since it can deal with comparatively high impeller-speeds, it requires a smaller pump chamber and as it hence also works without gear reduction, a gear-box is superfluous. Thus, the disc pump allows a small pump size for a given flow rate.
In the works of Blanchard Ligrani and Gale ([3], [4]), this type of micropump has been investigated both experimentally and analytically. In order to assess the pump performance and

for scaling-up/down purposes, it is important to characterize the pump with dimensionless coefficients. For a good choice of such coefficients, the behavior should be independent of the pump characteristic parameters, such as dimensions, rotational speed and used fluid. The presented set of coefficients satisfies this condition.
The article is organized as follows: In the first section the geometry and the functionality of the pump are explained. In the second section some remarks about the numerical modeling are made. In the third section, the flow results of the simulation of the pump are explained in detail. In the forth section the derivation of the scaling laws is presented.

1 Geometry and Functionality of the Pump

1.1 Geometry

The basic part of the minipump is a rotor mounted in a housing. The rotor consists of a circumferential slit in which the fluid can enter, move around and leave again. A wiper extends in the slit, to guide the fluid out of the pump. For a picture of the minipump see Figure 1 and for a front view (in the direction of the rotation axis) confer Figure 2.

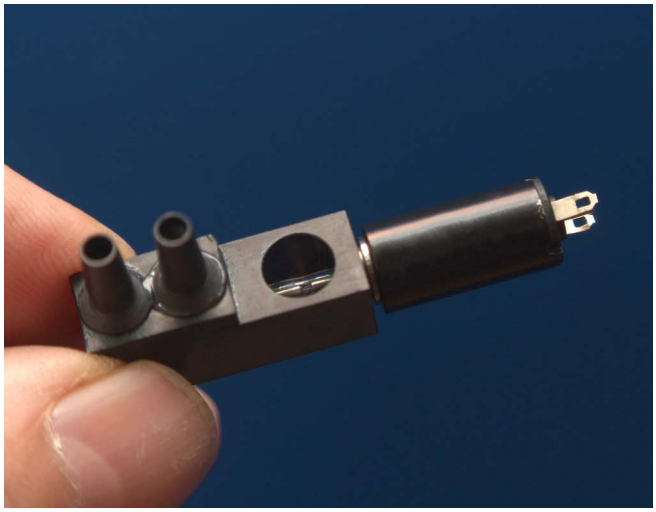

FIGURE 1. The minipump.

1.2 Fluid Domain of the Simplified Model

For simplification purposes only the slit was simulated in a so called simplified model. For a picture of the fluid domain of the simplified model see Figures 2 and 3.

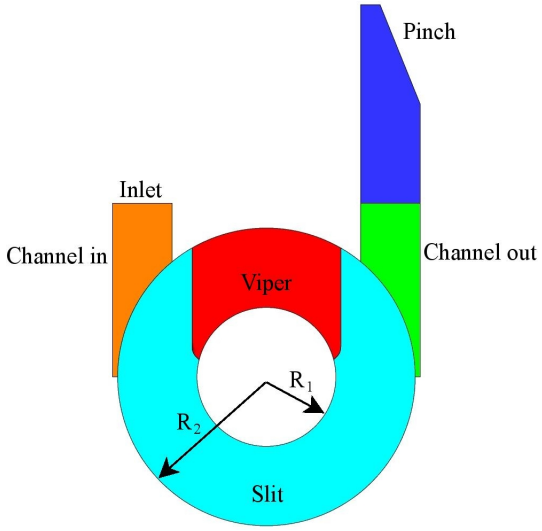

FIGURE 2. Geometry of the simplified model.

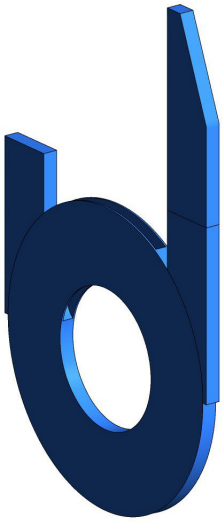

FIGURE 3. Fluid domain of the simplified model. A pinch at the outlet is attached at the outlet so as to produce realistic boundary conditions.

2 Numerical Modeling

2.1 Geometry and Mesh

The geometry of the numerically investigated disk pump has been simplified at the inlet and the outlet compared to the prototype. These two regions are not modeled as a reservoir like in reality but as frictionless extensions of the gap between the disks (see Figures 3 and 2). This simplifies the modeling procedure significantly but does not affect the results. In addition the outlet had to be pinched, in order to avoid backflow at the boundary, which would negatively affect the convergence. The meshes used

for the computations where generated with ICEM-CFD Hexa, allowing for high quality grids (cells angle and aspect ratio) and good resolution of the flow. The computational domain was resolved with 250000 nodes.

2.2 Software and Boundary Conditions

The computations were performed with ANSYS CFX V11, a commercial finite volume CFD code (confer [5]). The flow is laminar. The pump characteristic was computed for different rotor speeds and fluids (mainly change in viscosity), with at least 6 operating points on each speed line. At the inlet the velocity is prescribed and at the outlet the pressure.

3 Flow Results

3.1 Comparison between Simulation and Measurement

In Figure 4 the results from simulations and from measurements are plotted. The rotation speed is $n = 20000\,1/\text{min}$ and the medium is water. The geometry corresponds to the reference configuration ($B = 0.13\,\text{mm}$, $R_2 = 3\,\text{mm}$).

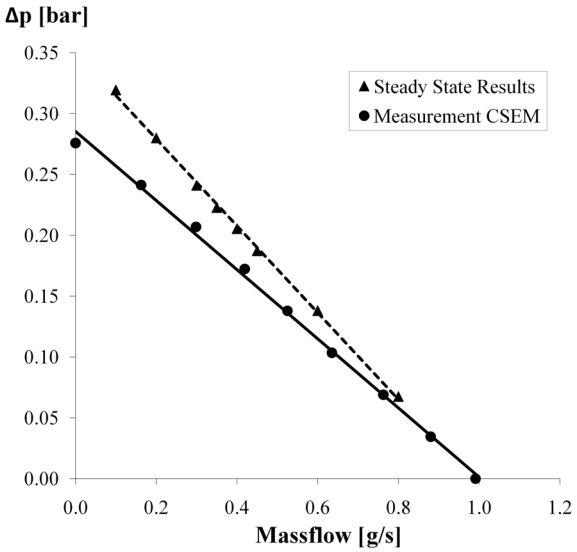

FIGURE 4. Comparison between simulation and measurement ($n = 20000\,1/\text{min}$, $B = 0.13\,\text{mm}$, $R_2 = 3\,\text{mm}$, the medium is water). The straight lines correspond to linear interpolations.

The slightly higher pressure rise in the simulations compared to the measurements can be explained by the fact that the leakage between the rotor and the housing was not part of the simulations. Another reason for the smaller pressure rise in the measurements is the pressure loss over the inlet and outlet channels, since in the measurements the pressure taps were placed further away from the rotor. The comparison shows as expected that the leakage is less important for smaller pressure rises.

3.2 CFD Results

The CFD results are presented for two different liquids, water and a 100 times more viscous fluid. The flow field for the two liquids shows quite different patterns, even if in both cases the flow is laminar. Only one operating point has been chosen.

Water: *Re*, based on gap width, of $O(100)$. In the case of water the isobars are curved, showing a mix between pressure increases along the radius, as it can be expected for a swirling flow, and along the flow path, due to the energy transfer from the rotor. A secondary flow in the channel cross section was detected, typical for enclosed disk flow, like it can be found in macroscopic devices as gas turbines (confer for example [6]). Along the rotating walls the flow moves outwards due to the centrifugal forces and in the center towards smaller radii. This can be clearly seen in the streamline plot in the midplane, where the flow moves toward the center. A back flow zone has been detected close to the rotor inner wall. For these fluid particles the pressure increase along the flow path is too strong, even if delayed compared to that at larger radii, thus leading to backflow. The momentum given by the inner cylindrical part of the rotor is not enough to compensate the pressure gradient.

High viscosity fluid: *Re*, based on gap width, of $O(1)$. In this fluid the isobars are straight and radially oriented. In contrary to water, no secondary flow was detected. This is mainly due to the fact that at this Re number the viscous forces are dominating the flow, thus inhibiting any sort of cross flow. All the fluid between the disks is moving in the same way, similarly to a solid. Therefore the pressure increase is not governed by centrifugal forces but only by the work input of the rotor along the path, thus leading to the observed pressure distribution. The streamlines in the midplane are nearly concentric, i.e. the radial component of the velocity is zero.

It is interesting to note, that at this high viscosity the inlet region into the disk presents a recirculation zone. According to the above explanation, the fluid between the disks moves "in one piece", thus leading to a blockage as soon as enough fluid has been sucked in the pump, depending on the specified operating point Looking carefully at all the pictures of the high viscosity fluid, where the *Re* based on the gap width is approximately 1, a symmetry along the vertical axis can be observed. It is almost not possible to say in which direction the flow is moving. This behavior is similar to that observed for other very low *Re* number flows, like the flow past immersed bodies (confer for example [7]). Also in this case a backflow region was detected close to the rotor inner wall. The radial extension is similar to that with water, indicating that basically the same mechanism is at the ori-

gin.
The features detected in the flow field are similar and in agreement with the description found in [3] which is based on measurements and flow visualization.

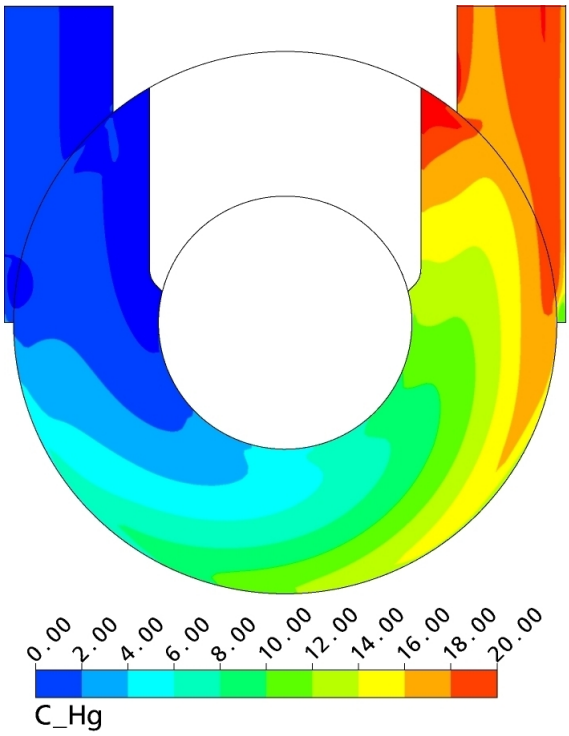

FIGURE 5. $C_{H,g}$, water.

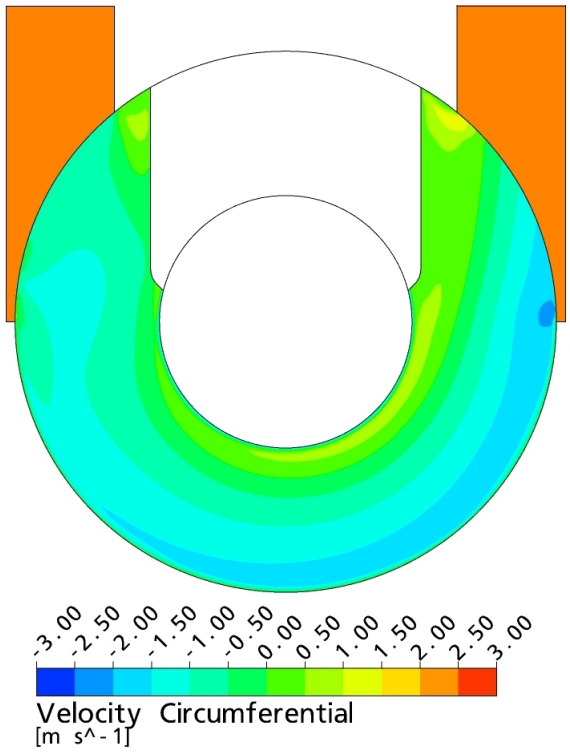

FIGURE 6. Circumferential velocity, water.

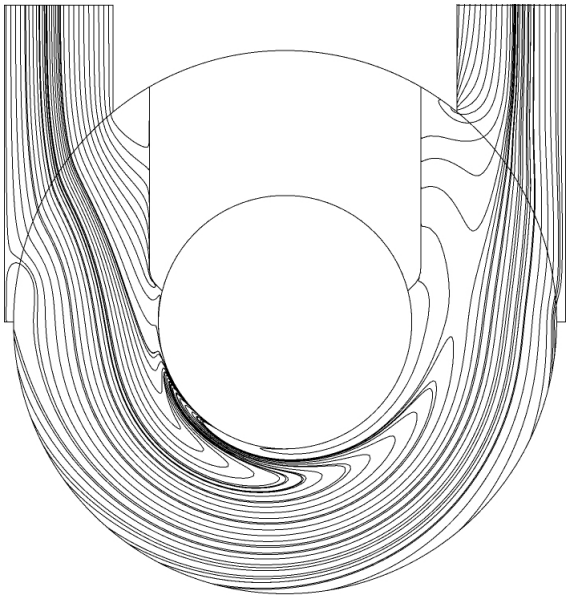

FIGURE 7. Streamlines water.

4 Dimensionless Analysis of the Results

Analysis and comparison of different pumps and in general turbomachines is usually performed using non-dimensional coefficients (as for example in [8]). For the present pump a typical turbomachinery approach was not successful, so that a new set of dimensionless coefficients for the mass flow and the hydraulic head has been derived.

4.1 Dimensionless Coefficients without including different Scaling in Radial and Axial Direction

4.1.1 Dimensionless Massflow In the following derivation D is a characteristic length (for example the diameter of the rotor).

$$Q \propto \rho w D^2 \propto \rho D^3 n, \tag{1}$$

where $w \propto nD$. One now defines the dimensionless massflow coefficient (in analogy to turbomachinery) as

$$C_Q := \frac{Q}{nD^3\rho} \tag{2}$$

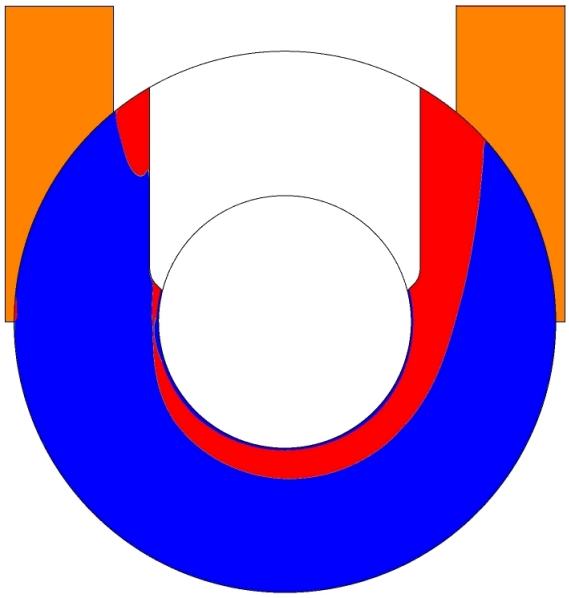

FIGURE 8. Backflow, water.

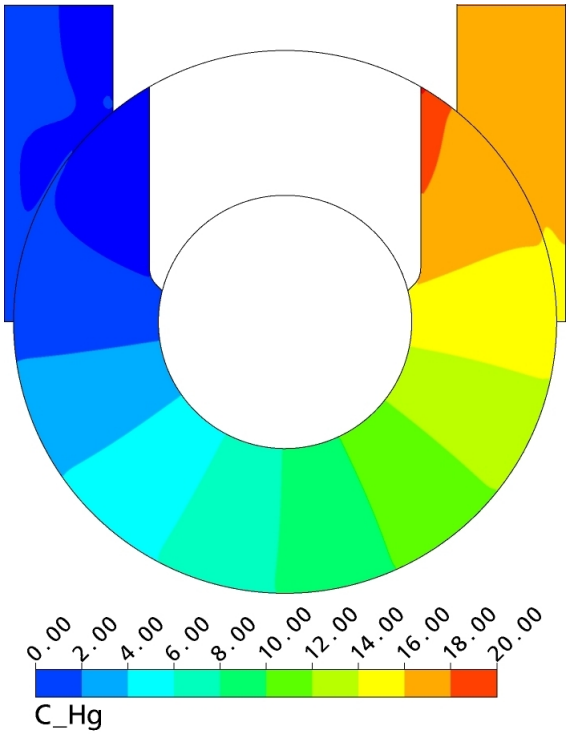

FIGURE 9. $C_{H,g}$, $\eta = 100\,\mathrm{mPas}$.

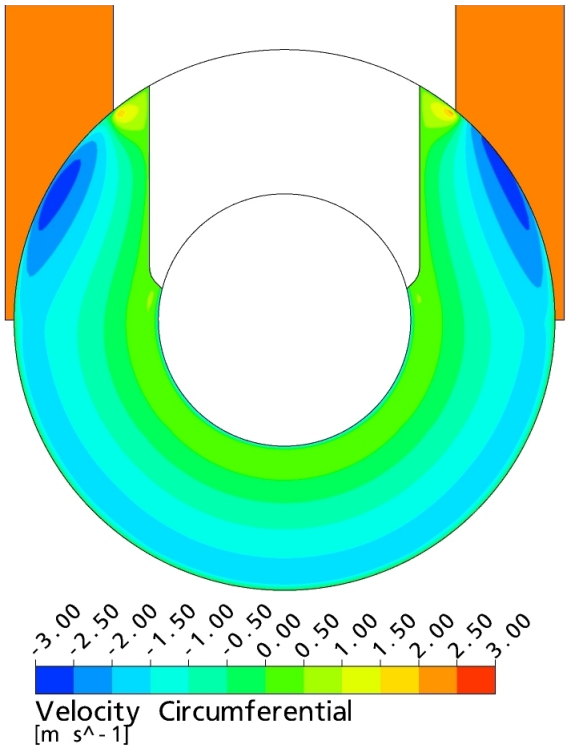

FIGURE 10. Circumferential velocity, $\eta = 100\,\mathrm{mPas}$.

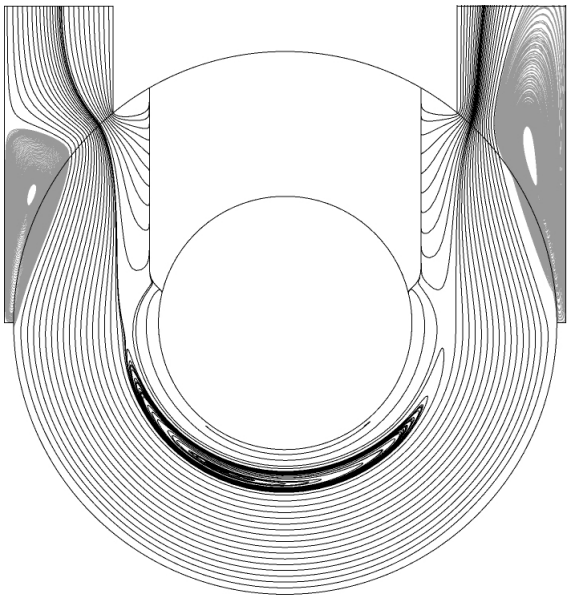

FIGURE 11. Streamlines, $\eta = 100\,\mathrm{mPas}$.

4.1.2 Dimensionless Hydraulic Head For laminar flow between two parallel plates, (Couette flow, see for example [9]), the following expressions for the force, torque and power can be derived:

$$F \propto \frac{w}{D}\eta D^2 = w\eta D. \tag{3}$$

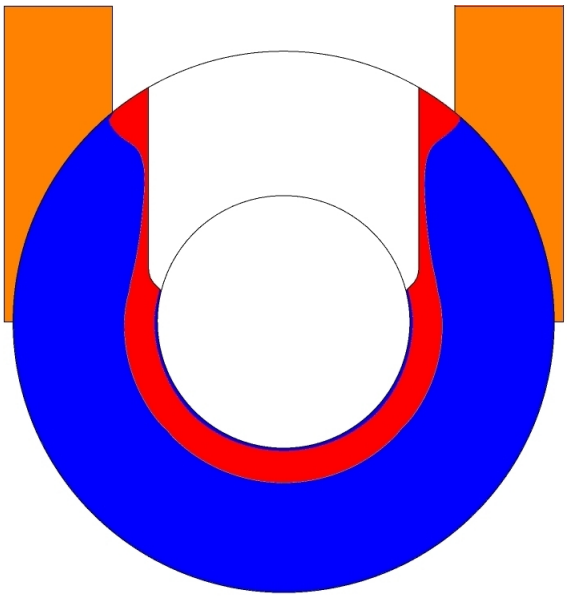

FIGURE 12. Backflow, $\eta = 100\,\mathrm{mPas}$.

$$M \propto FD \propto w\eta D^2. \tag{4}$$

$$P \propto M\omega \propto w\eta n D^2. \tag{5}$$

The specific work is then given as

$$Y = \frac{P}{Q} \propto \frac{w\eta n D^2}{w\rho D^2} \propto \frac{\eta n}{\rho} \tag{6}$$

Now one defines the dimensionless Head coefficient as

$$C_H := \frac{Y\rho}{\eta n} = \frac{\Delta p_{tot}\rho}{\rho\eta n} = \frac{\Delta p_{tot}}{\eta n} = \frac{gH_f\rho}{\eta n}, \tag{7}$$

where $\Delta p_{tot} = H_f g\rho$ and $Y = gH_f$.

4.2 Dimensionless Coefficients including different Scaling in Radial and Axial Direction, heuristic Approach

In this section a set of new dimensionless coefficients is defined in a more general way, taking into account all the characteristic dimensions of the pump.

4.2.1 Dimensionless Massflow In the following derivation D is a characteristic length in the radial direction and b is a characteristic length in the axial direction (gap direction).

$$Q \propto \rho wDb \propto \rho D^2 bn, \tag{8}$$

where $w \propto nD$ (assumption of circumferential flow). One now defines the dimensionless massflow coefficient as

$$C_{Q,g} := \frac{Q}{nD^2 b\rho} \tag{9}$$

4.2.2 Hydraulic Head For laminar flow between two parallel plates, (Couette flow, see for example [9]), it holds that

$$F \propto \frac{w}{b}\eta D^2 \propto w\eta\frac{D^2}{b}, \tag{10}$$

where it is assumed that the velocity is always in the circumferential direction. Therefore, the gradient of the velocity which scales as the characteristic length in the radial direction leads only to forces that act on the fluid to deflect it from a linear trajectory to a circular one. Calculating the torque gives

$$M \propto FD \propto w\eta\frac{D^3}{b}. \tag{11}$$

Therefore the power and the specific work are given as

$$P \propto M\omega \propto w\eta n\frac{D^3}{b}. \tag{12}$$

$$Y = \frac{P}{Q} \propto \frac{w\eta n}{w\rho}\frac{D^2}{b^2} \propto \frac{\eta n}{\rho}\left(\frac{D}{b}\right)^2 \tag{13}$$

Now one defines the dimensionless Head coefficient including all the characteristic lengths as

$$C_{H,g} := \frac{Y\rho}{\eta n}\left(\frac{b}{D}\right)^2 = \frac{\Delta p_{tot}\rho}{\rho\eta n}\left(\frac{b}{D}\right)^2 \tag{14}$$

$$= \frac{\Delta p_{tot}}{\eta n}\left(\frac{b}{D}\right)^2 = \frac{gH_f\rho}{\eta n}\left(\frac{b}{D}\right)^2, \tag{15}$$

where $\Delta p_{tot} = H_f g\rho$ and $Y = gH_f$.

The dimensionless results using the coefficients $C_{Q,g}$ and $C_{H,g}$ are presented in Figure 13.

In the work of Blanchard, Ligrani and Gale [4], they derive an

equation relating the pump head and the massflow (eq. 10), which reflects the behavior of their pump very well. The dimensionless coefficients derived in this article show similar dependencies.
The operating points of Blanchard Ligrani and Gale are included in Figure 13. The slope given by these two points is clearly less than the one of the here investigated micropump. The main reasons for this difference should be the path angle along the pump (in our case close to 180 degrees, in Blanchard about 90 degrees) and the wiper shape.

4.3 Dimensionless Coefficients including different Scaling in Radial and Axial Direction, rigorous Approach

The axis of rotation is chosen to be the z axis to meet the standard notation used when working in cylindrical coordinates. The components of the stress tensor in cylindrical coordinates are given as follows (confer [10])

$$\sigma_{rr} = -p + 2\eta \frac{\partial v_r}{\partial r} \tag{16}$$

$$\sigma_{\phi\phi} = -p + 2\eta \left(\frac{1}{r}\frac{\partial v_\phi}{\partial \phi} + \frac{v_r}{r} \right) \tag{17}$$

$$\sigma_{zz} = -p + 2\eta \frac{\partial v_z}{\partial z} \tag{18}$$

$$\sigma_{\phi r} = \eta \left(\frac{1}{r}\frac{\partial v_r}{\partial \phi} + \frac{\partial v_\phi}{\partial r} - \frac{v_\phi}{r} \right) \tag{19}$$

$$\sigma_{\phi z} = \eta \left(\frac{\partial v_\phi}{\partial z} + \frac{1}{r}\frac{\partial v_z}{\partial \phi} \right) \tag{20}$$

$$\sigma_{zr} = \eta \left(\frac{\partial v_z}{\partial r} + \frac{\partial v_r}{\partial z} \right) \tag{21}$$

The first assumption on the flow field is that the velocity is always directed in the circumferential direction. Therefore

$$v_r \equiv 0 \qquad \text{and} \qquad v_z \equiv 0. \tag{22}$$

The second assumption on the flow field is that the circumferential velocity does not depend on the angle

$$v_\phi = v_\phi(r,z). \tag{23}$$

These two assumptions already simplify the first three components of the fluid tensor to

$$\sigma_{rr} = \sigma_{zz} = \sigma_{\phi\phi} = -p. \tag{24}$$

Therefore, there are only pressure forces acting in the three normal directions on a fluid element. Pressure forces are not relevant for the transport of the fluid when it moves in the slit, only for the transport of the fluid into the slit and out of it at the entrance and the exit of the slit (see also [3]).
The assumptions also force the last component of the fluid tensor to vanish

$$\sigma_{zr} \equiv 0. \tag{25}$$

The third assumption on the flow field is that the velocity profile in the slit can be written in the following form

$$v_\phi = \tilde{f}(\alpha,\beta) n r, \tag{26}$$

where

$$\alpha := \frac{r}{R_2} \qquad \text{and} \qquad \beta := \frac{z}{b} \tag{27}$$

are normalized radial and axial coordinates and $\tilde{f}(\alpha,\beta)$ is a normalized function that describes the velocity profile in the slit just geometrically. It is defined by

$$\tilde{f}(\alpha,\beta) := f(\alpha R_2, \beta b) = f(r,z), \tag{28}$$

where $f(r,z)$ describes the actual velocity profile. It is assumed that the geometric shape of the velocity profile is independent of the actual dimensions of the slit and this is expressed by the form in equation 26. Since

$$r \in [0, R_2] \qquad \text{and} \qquad z \in [0, b] \tag{29}$$

it follows that

$$\alpha \in [0,1] \qquad \text{and} \qquad \beta \in [0,1]. \tag{30}$$

The properties of the normalized function $\tilde{f}(\alpha,\beta)$ can be imagined as follows: (For simplicity, the explanations at this point correspond only to a function of one variable, for example z. Nevertheless, the situation can be extended to two variables easily). Let a velocity profile be given. Using equation 26, this velocity profile corresponds to a function $f(z)$, where $z \in [0,b]$ (b is the width of the slit). To keep now exactly the same geometric shape when the geometry is scaled one normalizes the function as follows

$$\tilde{f}(\beta) := f(\beta b) = f(z). \tag{31}$$

If now b is changed then the shape of the velocity profile is kept since the argument of the function $\tilde{f}$ is always in $[0,1]$.

With this assumption, the fourth component of the fluid tensor is given as

$$\sigma_{\phi r} = \eta\left(\frac{1}{r}\frac{\partial v_r}{\partial \phi} + \frac{\partial v_\phi}{\partial r} - \frac{v_\phi}{r}\right) \tag{32}$$

$$= \eta\left(\frac{\partial \tilde{f}(\alpha,\beta)}{\partial r} nr + \tilde{f}(\alpha,\beta)n - \frac{\tilde{f}(\alpha,\beta)nr}{r}\right) \tag{33}$$

$$= \eta n\left(\frac{\partial \tilde{f}(\alpha,\beta)}{\partial \alpha}\frac{\partial \alpha}{\partial r}\right) r \tag{34}$$

$$= \eta n\left(\frac{\partial \tilde{f}(\alpha,\beta)}{\partial \alpha}\right)\frac{r}{R_2}, \tag{35}$$

where the factor $1/R_2$ is due to the chain rule. The fifth component of the fluid tensor is given as

$$\sigma_{\phi z} = \eta\left(\frac{\partial v_\phi}{\partial z} + \frac{1}{r}\frac{\partial v_z}{\partial \phi}\right) \tag{36}$$

$$= \eta n\left(\frac{\partial \tilde{f}(\alpha,\beta)}{\partial z}\right) r \tag{37}$$

$$= \eta n\left(\frac{\partial \tilde{f}(\alpha,\beta)}{\partial \beta}\right)\frac{r}{b}, \tag{38}$$

where the factor $1/b$ is also due to the chain rule.

Since $r \gg b$ and since the terms in the brackets in the equation 35 and 38 are assumed to be of the same order (they also don't scale because of the normalization of the function $\tilde{f}$), one concludes that $\sigma_{\phi z} \gg \sigma_{\phi r}$ (it is also used that R_2 and r are of the same order).

The fourth and the fifth component of the fluid tensor give a contribution to the force in the circumferential direction. This force leads then to a torque and so forth.

The force responsible for the torque is therefore given as

$$F_\phi \propto \sigma_{\phi z} D^2 \propto \eta n \frac{D^3}{b}, \tag{39}$$

where D is a characteristic length of the system in the radial direction (r, R_1 and R_2 scale as D). Following the same procedure as in the previous section leads to the following identities for the torque, power, massflow and specific work.

$$M \propto F_\phi D \propto \eta n \frac{D^4}{b}. \tag{40}$$

$$P \propto M\omega \propto \eta n^2 \frac{D^4}{b}. \tag{41}$$

$$Q \propto \rho b D v_\phi \propto \rho b D^2 n, \tag{42}$$

$$Y \propto \frac{P}{Q} \propto \frac{\eta n}{\rho}\left(\frac{D}{b}\right)^2. \tag{43}$$

Reformulating this in form of the rise of the total pressure $\Delta p_{tot} = \rho Y$ gives

$$\frac{\Delta p_{tot}}{\eta n}\left(\frac{b}{D}\right)^2 \propto \text{const.} \tag{44}$$

One therefore defines the dimensionless Head coefficient that includes the geometry by

$$C_{H,g} := \frac{\Delta p_{tot}}{\eta n}\left(\frac{b}{D}\right)^2 \tag{45}$$

The relative importance of the two terms $\sigma_{\phi z}$ and $\sigma_{\phi r}$ that give a contribution to the force in circumferential direction can be seen by keeping both terms in the analysis for the force (instead of just $\sigma_{\phi z}$ as in equation 39). With $F_{\phi z}$ as the force resulting from $\sigma_{\phi z}$ and $F_{\phi r}$ as the force resulting from $\sigma_{\phi r}$ one has

$$F_{\phi z} \propto \eta n \frac{D^3}{b} \qquad F_{\phi r} \propto \sigma_{\phi r} D b \propto \eta n D b, \tag{46}$$

where for the force $F_{\phi r}$ it was used that R_2 and r are subjected to the same scaling (confer equation 35) and that the surface in the ϕ-r-direction scales as Db. In terms of the fraction (b/D) this can be written as

$$F_{\phi z} \propto \eta n D^2 \left(\frac{b}{D}\right)^{-1} \qquad F_{\phi r} \propto \eta n D^2 \left(\frac{b}{D}\right). \tag{47}$$

The total force F_ϕ in circumferential direction is the sum of $F_{\phi z}$ and $F_{\phi r}$. Since one only has a description of the forces in terms of proportionalities, two additional constants appear in the sum. Those constants shall be called α and β.

$$F_\phi = F_{\phi z} + F_{\phi r} = \eta n D^2 \left(\alpha\left(\frac{b}{D}\right)^{-1} + \beta\left(\frac{b}{D}\right)\right). \tag{48}$$

According to this, it can be seen that in a regime where $b \ll D$, the first term clearly dominates. But for a growing fraction b/D,

this term becomes negligible and the second term dominates. Therefore, the scaling law derived above is a good approximation only in a certain geometric regime. For the simulations, the following fractions b/D are present

$$\frac{b}{D} \in \{0.0144, 0.0217, 0.05, 0.087\}. \tag{49}$$

The dimensionless results of the simulations are presented in Figure 13 where it was set $b = B$ and $D = R_2$ in the equations for the coefficients. Remark: In the geometric regime where b is of the same order as D, equation 48 yields the same coefficients as in section 4.1.

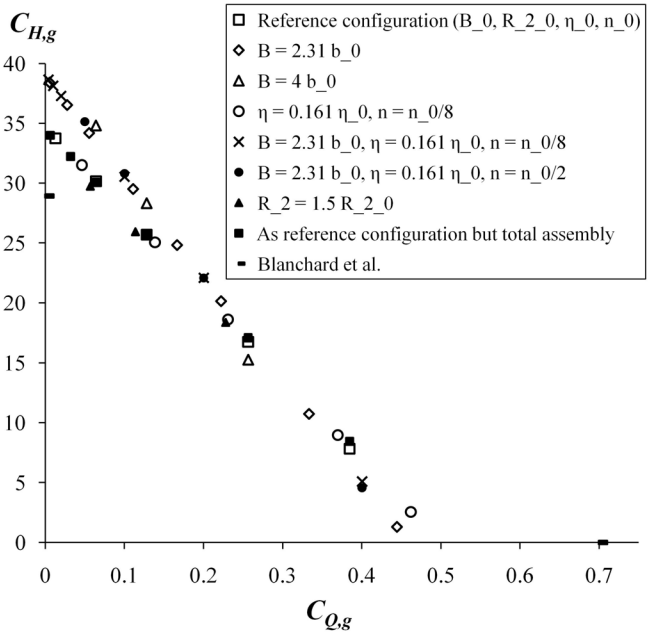

FIGURE 13. Dimensionless exposition of the results for different parameters. Where $C_{Q,g}$ is defined in equation 9 and $C_{H,g}$ is defined in equation 15. Here for the characteristic length in the axial direction R_2 is used and for the characteristic length in the axial direction B is used. The reference configuration corresponds to: $B_0 = 0.13\,\text{mm}$, $R_{2,0} = 3\,\text{mm}$, $\eta_0 = 100\,\text{mPas}$ and $n_0 = 20000\,1/\text{min}$.

4.4 Explanation of the different Slopes and y-Intercepts in Figure 13

One now has two different pairs of coefficients for two different geometric regimes. The first regime is the regime where $b \ll D$ which is also the regime where disk pumps work. In this regime one has the two dimensionless coefficients

$$C_{Q,g} := \frac{Q}{nD^2 b\rho} \qquad \text{and} \qquad C_{H,g} := \frac{\Delta p_{tot}}{\eta n}\left(\frac{b}{D}\right)^2. \tag{50}$$

In order to understand the slope change in the characteristic, the analysis is extended to a second hypothetical regime, given when b and D are of the same order. In this regime one has the following pair of coefficients

$$\tilde{C}_{Q,g} := \frac{Q}{nD^2 b\rho} \qquad \text{and} \qquad \tilde{C}_{H,g} := \frac{\Delta p_{tot}}{\eta n}. \tag{51}$$

One now assumes, that for both geometric regimes one has a linear correspondence between the head coefficient and the mass-flow coefficient (this assumption is clearly met in the first regime (confer Figure 13)). Therefore one has two linear equations which are satisfied in the corresponding regime

$$C_{H,g} = \gamma C_{Q,g} + \delta \quad \text{for} \quad b \ll D \tag{52}$$

$$\tilde{C}_{H,g} = \tilde{\gamma}\tilde{C}_{Q,g} + \tilde{\delta} \quad \text{for} \quad b, D \text{ of the same order.} \tag{53}$$

One now wants to know what happens if one is in the regime where b and D are of the same order, but one still wants to use the description from the regime where $b \ll D$. One knows that (confer the equations 50 and 51)

$$\tilde{C}_{H,g} = \left(\frac{D}{b}\right)^2 C_{H,g}. \tag{54}$$

Therefore

$$C_{H,g} = \left(\frac{b}{D}\right)^2 \tilde{C}_{H,g} = \left(\frac{b}{D}\right)^2 \left(\tilde{\gamma} C_{Q,g} + \tilde{\delta}\right) = \gamma C_{Q,g} + \delta, \tag{55}$$

where for the second equality the fact is used that one is in the regime where b and D are of the same order and therefore can make use of the linear equation 53. For the third equality one defines

$$\gamma := \left(\frac{b}{D}\right)^2 \tilde{\gamma} \qquad \text{and} \qquad \delta := \left(\frac{b}{D}\right)^2 \tilde{\delta} \tag{56}$$

to meet the linear form as desired.

Now it follows, that if one is in the regime where b is of the same order as D but one expresses the relation between the

head coefficient and the massflow coefficient in the form of the other regime, then for a larger fraction b/D, the slope γ of the description is larger and the y-intercept δ of the description is also larger.

With this idea, the different slopes and y-intercepts in Figure 13 can be explained properly. For the four different ratios b/D (confer equation 49), the linearly interpolated results are presented in Figure 14. For a larger b at a constant D, the b/D ratio grows. Therefore, the description used in Figure 13 becomes more and more inappropriate and leads to larger and larger slopes and y-intercepts. The different slopes corresponding to the different ratios b/D are illustrated in Figure 14

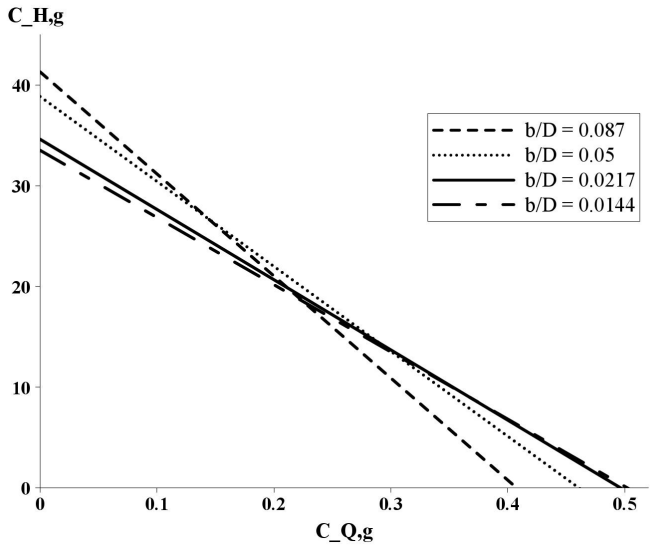

FIGURE 14. Linear interpolated exposition of the dimensionless results for the four different ratios $b/D \in \{0.087, 0.05, 0.0217, 0.0144\}$.

5 Conclusions

The paper presents a detailed flow field analysis of a disk micropump.
Even if for the investigated fluids the flow is always laminar, important differences in the flow field were detected. In order to characterize the pump performance, a dimensionless set of coefficients has been derived. The application of these coefficients for different pump configurations, where parameters as fluid and geometry were varied, shows the good results of the new correlation. This is well suited for scale up purposes.

REFERENCES

[1] Iverson, B., and Garimella, S., 2008. Recent Advances in Microscale Pumping Technologies: A Review and Evaluation.

[2] Amirouche, F., Zhou, Y., and Tom, J., 2009. Current Micropump technologies and their biomedical application.

[3] Blanchard, D., Ligrani, P., and Gale, B., 2005. Single-disk and double disk viscous micropumps.

[4] Blanchard, D., Ligrani, P., and Gale, B., 2006. Miniature Single-Disk Viscous Pump (Single-DVP), Performance Characterization.

[5] *ANSYS CFX V11 User Manual*.

[6] Daily, J., and Nece, R., 1960. Chamber dimension effects on induced flow and frictional resistance of enclosed rotating disks.

[7] VanDyke, M., 1982. *Album of Fluid Motion*, 10th ed. Parabolic Press, Inc., 6.

[8] Pfleiderer, C., and Petermann, H., 2004. *Stroemungsmaschinen (Klassiker der Technik) (German Edition)*, 7., unvernd. auflage ed. Springer, 10.

[9] White, F. M., 2007. *Fluid Mechanics (6th International Edition)*. McGraw-Hill.

[10] Landau, L. D., and Lifshitz, E. M., 1987. *Course of Theoretical Physics, Vol.6 : Fluid Mechanics*, 0002 ed. Butterworth Heinemann, 1.